Ultrahigh Sensitivity of Au/1D α-Fe 2 O 3 to Acetone and the Sensing Mechanism

7 AUTHORS, INCLUDING:

Poernomo Gunawan
Institute of Chemical and Engineering Sciences
25 PUBLICATIONS **910** CITATIONS

SEE PROFILE

Jianmin Ma
Lanzhou University
79 PUBLICATIONS **1,384** CITATIONS

SEE PROFILE

James George Highfield
Agency for Science, Technology and Research …
61 PUBLICATIONS **1,362** CITATIONS

SEE PROFILE

Ziyi Zhong
Institute of Chemical and Engineering Sciences
185 PUBLICATIONS **5,196** CITATIONS

SEE PROFILE

# Ultrahigh Sensitivity of Au/1D α-Fe$_2$O$_3$ to Acetone and the Sensing Mechanism

Poernomo Gunawan,[†] Lin Mei,[‡] Jaclyn Teo,[†] Jianmin Ma,[‡] James Highfield,[†] Qiuhong Li,*[,‡] and Ziyi Zhong*[,†]

[†]Institute of Chemical and Engineering Sciences, A*Star, 1 Pesek Road, Jurong Island, Singapore 627833

[‡]Key Laboratory for Micro-Nano Optoelectronic Devices of Ministry of Education, State Key Laboratory for Chemo/Biosensing and Chemometrics, Hunan University, Changsha, China 410082

S *Supporting Information*

ABSTRACT: Hematite (α-Fe$_2$O$_3$) is a nontoxic, stable, versatile material that is widely used in catalysis and sensors. Its functionality in sensing organic molecules such as acetone is of great interest because it can result in potential medical applications. In this report, microwave irradiation is applied in the preparation of one-dimensional (1D) α-FeOOH, thereby simplifying our previous hydrothermal method and reducing the reaction time to just a few minutes. Upon calcination, the sample was converted to porous α-Fe$_2$O$_3$ nanorods, which were then decorated homogeneously by fine Au particles, yielding Au/1D α-Fe$_2$O$_3$ at nominally 3 wt % Au. After calcination, the sample was tested as a potential sensor for acetone in the parts per million range and compared to a similarly loaded Pt sample and the pure 1D α-Fe$_2$O$_3$ support. Gold addition results in a much enhanced response whereas Pt confers little or no improvement. From tests on acetone in the 1−100 ppm range in humid air, Au/1D α-Fe$_2$O$_3$ has a fast response, short recovery time, and an almost linear response to the acetone concentration. The optimum working temperature was found to be 270 °C, which was judged to be a compromise between the thermal activation of lattice oxygen in hematite and the propensity for acetone adsorption. The surface reaction was investigated by diffuse reflectance infrared Fourier transform spectroscopy (DRIFTS), and a possible sensing mechanism is proposed. The presence of Au nanoparticles is believed to promote the dissociation of molecular oxygen better in replenishing O vacancies, thereby increasing the instantaneous supply of lattice oxygen to the oxidation of acetone (to H$_2$O and CO$_2$), which proceeds through an adsorbed acetate intermediate. This work contributes to the development of next-generation sensors, which offer ultrahigh detection capabilities for organic molecules.
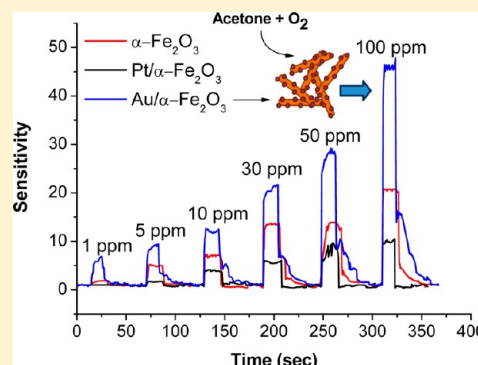
1. INTRODUCTION

Hematite (α-Fe$_2$O$_3$) is a cheap, stable, environmentally benign compound that is widely used in catalysis,[1] pigments,[2] lithium ion batteries,[3] and gas sensors.[4] In recent years, efforts have been made to prepare this material in improved (textural) forms for such applications. For example, various one-dimensional (1D) α-Fe$_2$O$_3$ nanostructures such as nanorods, nanowires, and nanotubes have been reported,[5] with beneficial attributes such as a high surface area and porosity. Our previous results show that, when decorated with fine gold (Au) particles, porous and 1D α-Fe$_2$O$_3$ is superior to the commercial Fluka α-Fe$_2$O$_3$ in CO oxidation at room temperature.[6] Elsewhere, it has been found that porous α-Fe$_2$O$_3$ nanoplates exhibit high sensitivity to acetone molecules.[7]

Synthesis methods for hematite include vacuum pyrolysis,[5a] sol−gel,[5b] and conventional hydrothermal techniques,[5c,d] with or without using structural directing agents such as alkylamines[5d] and tetraethylammonium hydroxide (TEAOH).[6] In contrast to these conventional methods, microwave irradiation is simple, fast, and energy efficient.[8] Furthermore, it offers better control over the local reaction

environment because of its internal heating mechanism. Therefore, a much more uniform nucleation environment is established, resulting in fast but well-controlled crystal growth.[9] Monodisperse α-Fe$_2$O$_3$ nanoparticles with various aspect ratios have been successfully synthesized by this microwave-assisted hydrothermal method.[10]

As an n-type semiconductor, one important application of iron(III) oxide is to act as a gas sensor, especially in environmental and clinical applications. Both α- and γ-Fe$_2$O$_3$ as well as their derivatives have been reported to exhibit good sensitivity toward several types of gases, such as ammonia, LPG, ethanol, and acetone, which can be important in various fields.[4,11] For instance, clinically they can be used as a medical diagnostic tool because a trace amount of acetone (<0.9 ppm) is found as a normal constituent in the expiration of a healthy person, whereas a higher value indicates a possible diabetic condition.[12] Earlier research has suggested that the analysis of

breath acetone may be more effective than urine sampling for monitoring ketosis in insulin-dependent diabetic patients with high levels of ketones.[13] Therefore, there is a need to develop novel sensor materials with high sensitivity for the parts per million-level detection of acetone. As demonstrated in our previous work, porous α-Fe$_2$O$_3$ is a good candidate for this application.[7]

The above sensing process with respect to organic molecules involves a number of oxidation reactions that consist of several elementary steps, including the activation of molecular oxygen (O$_2$) to form active oxygen species. It is well known that supported noble metal catalysts on metal oxide supports, such as α-Fe$_2$O$_3$, are very active in oxidative reactions, such as low-temperature CO oxidation.[14] Therefore, it is expected that the loading of a noble metal (e.g., Au, Pt) onto an oxide semiconductor should promote its sensitivity toward organic molecules. A recent paper by Zhang et al. reported the high sensitivity of Au/α-Fe$_2$O$_3$ nanospindles toward different organic gases, such as ethanol, ether, and acetone.[15]

Herein, we report a microwave-assisted hydrothermal method for the synthesis of 1D α-FeOOH as an important advancement of the previously reported method.[6] Microwave irradiation causes a drastic acceleration in the unidimensional growth rate. The obtained 1D α-FeOOH is subsequently converted to porous 1D α-Fe$_2$O$_3$ nanorods via calcination. Thereafter, small Au and Pt nanoparticles are deposited and their gas-sensing properties are examined using acetone as the probe molecule. A significant enhancement in the specific response to acetone is observed for Au-deposited mesoporous 1D α-Fe$_2$O$_3$. Tracing the surface chemistry by DRIFTS sheds valuable light on the oxidation pathway and how this relates to the sensing mechanism.

2. EXPERIMENTAL METHODS

2.1. Synthesis of Porous 1D α-Fe$_2$O$_3$. All chemicals were reagent grade and used without further purification. In a typical synthesis, 0.92 g (2.28 mmol) of Fe(NO$_3$)$_3$·9H$_2$O (98%, Strem Chemicals) was mixed with 10 mL (13.6 mmol) of tetraethylammonium hydroxide (TEAOH, 20% aq solution, Alfa Aesar), and the mixture was rigorously stirred for 20 min to allow dissolution and hydrolysis of the iron precursor. Subsequently, the solution was irradiated in a microwave oven. The power function was set at 10% of maximum power (max = 1 kW), and the irradiation times were 10, 20, 40, 60, 120, and 300 s. The precipitate was collected by centrifugation and thoroughly washed with ultrapure water to remove excess TEAOH. The recovered solid was then dried overnight in an oven at 60 °C. To obtain α-Fe$_2$O$_3$, the as-prepared goethite (FeOOH) was calcined at 250 or 400 °C for 1 h, respectively. It was found that the microwave irradiation time substantially influenced the yield of the 1D α-FeOOH product. For example, irradiation for 10 s yielded less than 2% of the theoretical weight of goethite, whereas a 300 s exposure raised the yield to 85 wt %. Therefore, unless otherwise mentioned, a 300 s irradiation time was applied as standard.

2.2. Deposition of Au (Pt) Nanoparticles on Porous 1D α-Fe$_2$O$_3$. The deposition of Au and Pt nanoparticles was carried out using our invented sonochemical method.[16] This produces small Au colloids via the reduction of HAuCl$_4$ with NaBH$_4$ in the presence of a capping reagent (lysine) and the support. During the reduction, ultrasonic irradiation (sonication) is applied, which efficiently facilitates the deposition of the Au colloids on the support. In a typical preparation, 500 mg of α-Fe$_2$O$_3$ was added to 10 mL of ultrapure water, followed by the addition of 9.0 mL of 0.01 M HAuCl$_4$ (99.99%, Premion, Alfa Aesar) and 9.0 mL of 0.01 M L-lysine (97%, SAFC, Sigma-Aldrich) to obtain a ca. 3 wt % Au loading. The pH value of the suspension was adjusted to 5 to 6 with 0.10 M NaOH, after which it was subjected to sonication for 20 s. During the sonication,

freshly prepared NaBH$_4$ (0.1 M, NaBH$_4$/Au molar ratio of 5−10) was injected instantaneously and the suspension immediately turned dark. After the sonication, the end-point pH value was measured to be 8 to 9. The solid was then collected by centrifugation and washed with ultrapure water four times. The entire procedure to obtain this catalyst, including the solution preparation and the washing cycles, took less than 1 h. The same procedure was also applied to prepare 3 wt % Pt/α-Fe$_2$O$_3$ by using H$_2$PtCl$_6$·6H$_2$O (99%, Sigma-Aldrich) as the Pt precursor.

2.3. Sensor Performance Measurement. The fabrication and testing principle of the gas sensor are similar to that described in our previous reports.[17] The Au/α-Fe$_2$O$_3$ samples were first mixed with terpineol to form a paste and then evenly coated on the outer surface of an alumina tube with a dip coating method; the thickness of the layer was around 200 μm. The diameter of the alumina tube is 1 mm, and the length is 5 mm. A piece of Ni−Cr alloy, inserted through the inner tube, was employed as a heater to control the operating temperature. To improve their stability and repeatability, the gas sensors were aged at 300 °C for 2 weeks in air. The detection properties of the sensors were measured with an NS-4003 series gas-sensing measurement system (China Zhong-Ke Micronano IOT, Internet of Things, Ltd.). The relative humidity (RH) was about 45%. The response and recovery times were defined as the times required for a change in the resistance to reach 90% of the equilibrium value after the detected gas was injected and removed, respectively. The sensor response (sensitivity, S) of the evaluated sensor is calculated using the following equation

$$S = \frac{R_a}{R_g}$$

where R_a is the sensor resistance in air at a particular temperature and R_g is the sensor resistance in the presence of the analyzed gas, in this case, acetone, at the same temperature.

2.4. Material Characterization. Powder X-ray diffraction (XRD) analysis was conducted on a Bruker D8 Advance X-ray diffractometer with Cu Kα1 radiation. The morphology and particle size of the products were observed with a transmission electron microscope (TEM, Tecnai TF20 Super Twin, 200 kV). A thermal analysis and decomposition study was performed on a TGA Q500 TA Instrument in air flow at a heating rate of 10 °C/min. The Fourier transform infrared (FTIR) spectra for powder samples were recorded on an FTS 3000MX Bio-Rad Excalibur spectrometer by employing a KBr pressed-disk method. The Brunauer−Emmett−Teller (BET) surface area was measured at 77 K (liquid nitrogen) on a Quantachrome Autosorb-6B surface area and pore size analyzer after prior degassing of the samples at 200 °C for several hours.

DRIFTS analysis was carried out on a Digilab Excalibur FTIR spectrometer. Prior to the analysis, the sample was thermally conditioned at 300 °C in flowing air for 1 h. Subsequently, the sample was cooled to room temperature, and acetone vapor was introduced into the DRIFTS cell at room temperature (RT), 200, 270, and 300 °C in step holds. The acetone vapor was generated via the bubbling of acetone liquid at 0 °C with a mixture of 50% by volume air in N$_2$ gas as the carrier.

Temperature-programmed reduction (TPR), using 2.5% CO in argon for all samples, was conducted on a Setaram Setsys 1200 thermobalance coupled through a heated transfer line to the heated gas cell in the FTIR spectrometer, operating in the kinetics mode of the Resolutions Pro software package. The total gas flow rate was 30 mL/min, and a heating ramp of 10 °C/min was applied up to 700 °C. An FTIR absorbance spectrum at 4 cm^{-1} resolution in the range of 4000−400 cm^{-1} was stored every minute (120 coadded scans), from which the recovery of CO$_2$ was monitored by the area under the bending vibration centered at 670 cm^{-1}. The conversion of CO was monitored by diminution in the area under the fundamental stretching envelope centered at 2140 cm^{-1}.
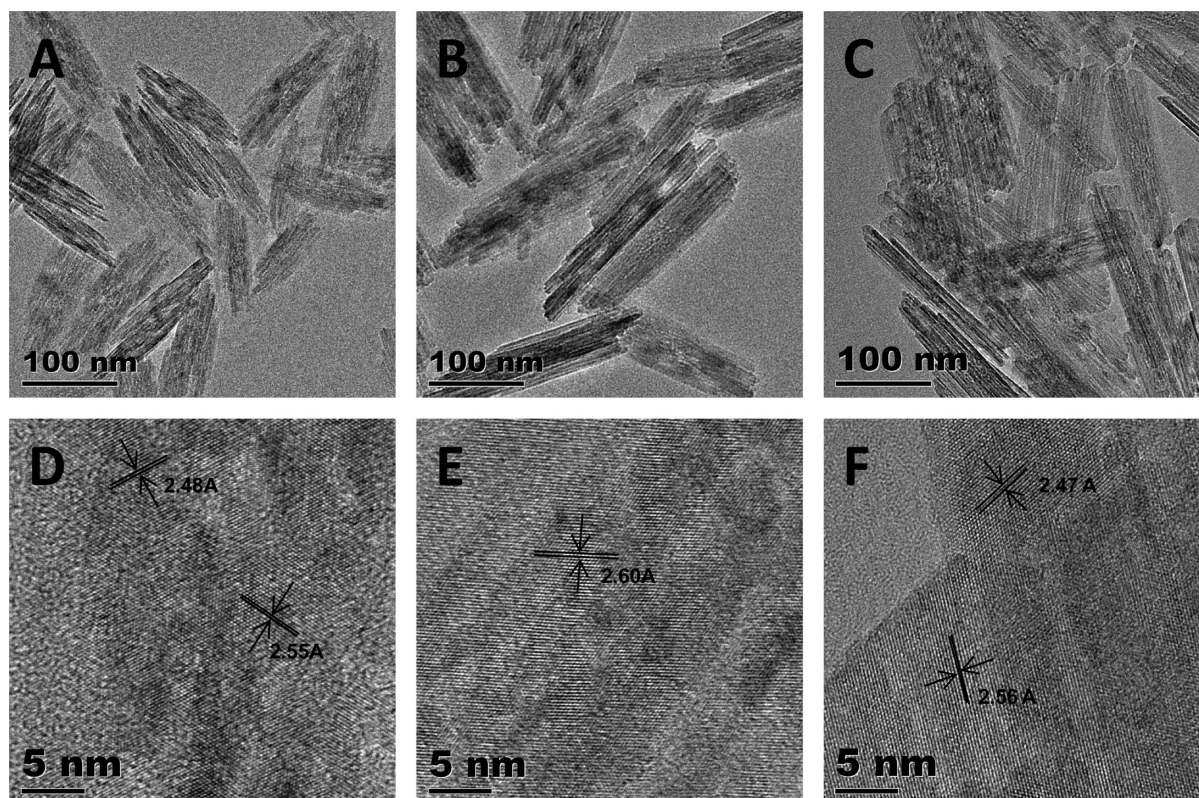
Figure 1. TEM images of FeOOH obtained under microwave irradiation at different times: (A, D) 10, (B, E) 60, and (C, F) 300 s.

3. RESULTS AND DISCUSSION

3.1. α-Fe$_2$O$_3$-Based Sensor Materials. The microwave irradiation-assisted synthesis was modified from our prior article[6] in which an excess amount of TEAOH (TEAOH/Fe = 6) was used as the structural directing agent to form 1D α-FeOOH. (See the XRD results in this section.) Figure 1 presents the TEM images of α-FeOOH obtained after microwave irradiation at low intensity (10%) for different periods (10, 60, and 300 s). The formation of α-FeOOH nanorods is a very fast process under microwave irradiation. As shown in Figure 1A, a short irradiation time (10 s) begins to generate the nanorods, albeit in low yield. It should be noted that the initial pH value of the solution was ca. 14 after the addition of TEAOH to the Fe(NO$_3$)$_3$ solution, which should be high enough for the hydrolysis of Fe(NO$_3$)$_3$ to form α-FeOOH fine particles. However, in the absence of microwave irradiation and a 24 h aging period at room temperature, the formation of 1D α-FeOOH was still not complete, as shown in Figure S1. Our previous results showed that the formation of 1D α-FeOOH took ca. 10 h at 40 °C.[6] These results clearly reveal that microwave irradiation dramatically accelerates the assembly of α-FeOOH nuclei into 1D α-FeOOH.

Upon closer observation, it was apparent that the samples consisted of bundles of small nanorods. Aggregation into these nanobundles indicated that the surface properties of individual nanorods were slightly hydrophobic. This is probably due to the dissociation of TEAOH into tetraethylammonium cations [(Et)$_4$N$^+$], which are attracted to the negatively charged iron oxide hydroxide particles.[6,18] Initially, the as-formed α-FeOOH nanoparticles were rather poorly crystallized and ill-defined (Figure 1A,D). Upon prolonged irradiation, the crystallinity increased and distinct nanorods were formed (Figure 1C,F). The average dimensions of an individual nanorod were about

6−10 nm diameter and 190−200 nm length, and those of the nanobundles were about 35−60 nm diameter and 180−230 nm length. The measured lattice plane distances of 2.47 and 2.56 Å obtained by HRTEM suggest that the crystal growth orientation is predominantly in the (111) and (021) directions, respectively. These values are in good agreement with those obtained from XRD.

From XRD (Figure 2), it was evident that the initial product was α-FeOOH (goethite) according to the standard card (JCPDS 00-029-0713). After calcination at 250 and 400 °C, the product was identified as hematite, α-Fe$_2$O$_3$ (JCPDS 00-033-0664), which exhibits a pattern similar to that of the commercial (Fluka) sample. Therefore, the as-prepared 1D
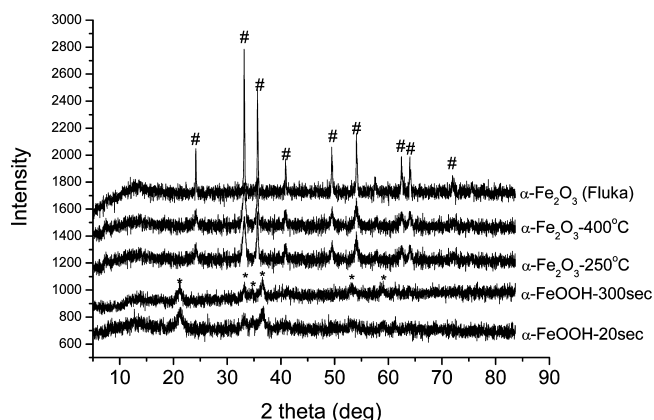

Figure 2. XRD patterns of FeOOH obtained at different microwave irradiation times of 20 and 300 s, the derived α-Fe$_2$O$_3$ after calcination at 250 and 400 °C for 1 h, and the commercial α-Fe$_2$O$_3$ (Fluka) (* indicates FeOOH, # indicates α-Fe$_2$O$_3$).
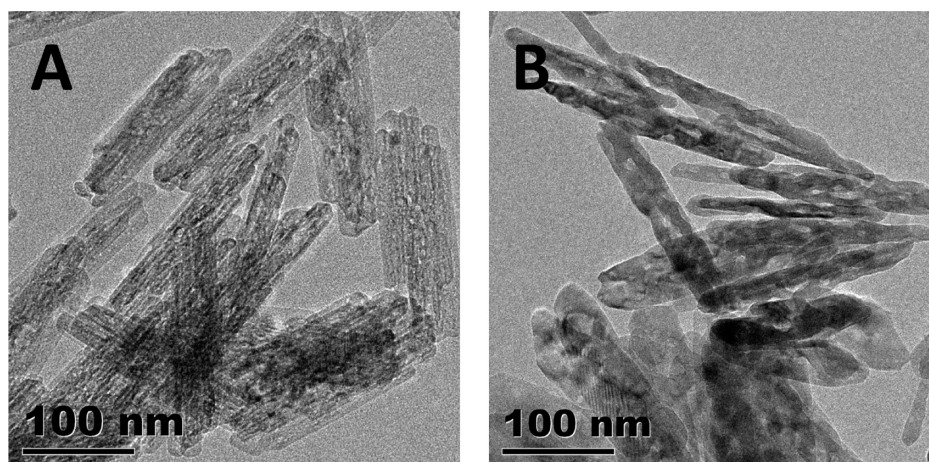
Figure 3. TEM images of porous α-Fe$_2$O$_3$ obtained at (A) 250 and (B) 400 °C.

iron oxide was structurally quite pure, showing no peaks due to typical impurities such as γ-Fe$_2$O$_3$ (maghemite) or Fe$_3$O$_4$ (magnetite).

As shown in Figure 3, the calcination of as-prepared α-FeOOH also results in the creation of nanopores in the final hematite product, probably owing to removal of the adsorbed TEAOH molecules and OH groups.[11c,19] Upon annealing, the 1D structure was evidently well maintained. At the lower calcination temperature (250 °C), small pores in the range of 1−5 nm were created (Figure 3A), whereas the higher temperature (400 °C) induced particle sintering and the formation of larger pores in the 5−15 nm range. The TEM observation is in good agreement with the BJH desorption pore distribution profile, which is 2.3 nm for the former and 10.2 nm for the latter (Figure S2). As observed in Figure 3B, the small FeOOH nanorods merged together to form larger α-Fe$_2$O$_3$ nanorods. TGA and FTIR analyses (Figure S3) show that the transformation of α-FeOOH to 1D α-Fe$_2$O$_3$ follows essentially the same pattern as the conventional hydrothermal method,[6] only at a much higher rate under microwave irradiation.

Subsequently, Au and Pt nanoparticles were deposited on porous α-Fe$_2$O$_3$ using the previously reported sonochemical method.[16a] Figure 4 presents the XRD patterns of pristine α-Fe$_2$O$_3$ along with the Au- and Pt-deposited α-Fe$_2$O$_3$. The formation of Au nanocrystals on α-Fe$_2$O$_3$ (3% Au/α-Fe$_2$O$_3$)

Figure 4. XRD patterns of calcined α-Fe$_2$O$_3$ at 250 °C (Fe-250) and 400 °C (Fe-400), 3% Au/α-Fe$_2$O$_3$ calcined at 250 °C (Au/Fe-250) and 400 °C (Au/Fe-400), and 3% Pt/α-Fe$_2$O$_3$ calcined at 250 °C (Pt/Fe-250) and 400 °C (Pt/Fe-400).

was evident from the appearance of the Au(111) diffraction peak at 38.2° (marked with *). The TEM image (Figure 5A) shows that the small (3−8 nm) Au nanoparticles were distributed homogeneously. In contrast, no X-ray diffraction peaks of metallic Pt were evident in the similarly loaded Pt/α-Fe$_2$O$_3$ sample. However, TEM (Figure 5B) showed evidence both for finely dispersed Pt domains and a few larger aggregates. Under high magnification (Figure 5B inset), the former were revealed as fine aggregates in the 1−4 nm range. SEM-EDX and XRF spectroscopy were used to determine the amount of deposited Au and Pt. From multiple-area sampling, SEM-EDX indicated a homogeneous distribution of Au with an average local loading of 3.3%, and XRF analysis gave a slightly lower amount of around 2.7 wt %. In contrast, the 3% Pt/α-Fe$_2$O$_3$ sample exhibited a nonuniform distribution of Pt nanoparticles, with an average Pt content of about 1.95% by XRF.

3.2. Gas-Sensing Performance. Au- and Pt-decorated 1D α-Fe$_2$O$_3$ samples were evaluated for their sensitivities toward acetone vapor and compared to that of the pure hematite support. To optimize the operating temperature to achieve the best sensing response, 100 ppm acetone was used as the standard, and the sample response was evaluated from 200 to 360 °C, as shown in Figure 6A. For simplification, α-Fe$_2$O$_3$ calcined at 400 °C is denoted as Fe-400, and its Au- and Pt-deposited samples are denoted as Au/Fe-400 and Pt/Fe-400, respectively. It was found that the maximum sensitivity for Fe-400 ($S = 20.9$) and Au/Fe-400 ($S = 46.4$) occurred at 270 °C whereas that for Pt/Fe-400 ($S = 10$) occurred at 300 °C. It is believed that as the temperature increases (from ambient) a higher response is observed because of the activation of adsorbed molecular oxygen and lattice oxygen to form active O_2^- and O^- and mobile O^{2-} species, respectively.[20] This phenomenon continues up to a certain optimum temperature, beyond which reactants begin to desorb in large quantities. Given its volatile nature, the steady-state level of adsorbed acetone molecules will decrease progressively with increasing temperature, leading to a drop in sensor response.[11d] Thus, the optimum temperature is a balance point between two conflicting mechanisms. The overall sensing performance for acetone levels from 1 to 500 ppm is summarized in Table 1. It can be seen that calcination at 400 °C resulted in consistently better detection sensitivity than calcination at 250 °C. Thus, the
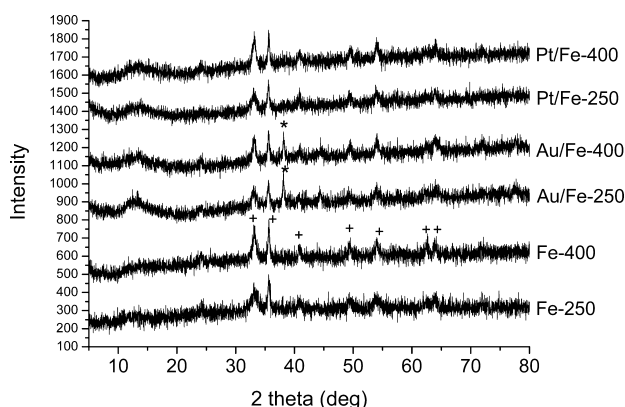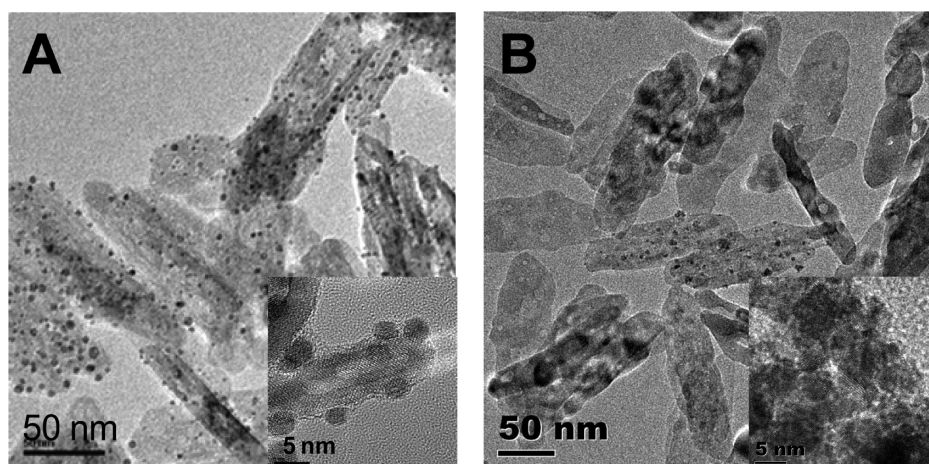
Figure 5. TEM images of (A) 3% Au/α-Fe$_2$O$_3$ and (B) 3% Pt/α-Fe$_2$O$_3$ calcined at 400 °C. The insets are the high-resolution TEM images for the respective samples.
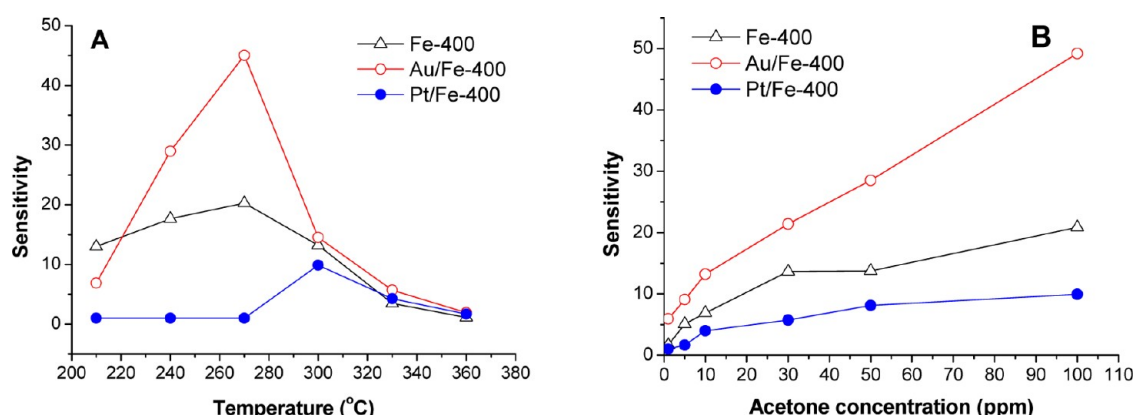

Figure 6. Sensor sensitivity at (A) different temperatures with a fixed acetone concentration at 100 ppm and (B) different acetone gas concentrations at the optimum operating temperatures: 270 °C for Fe-400 and Au/Fe-400 and 300 °C for Pt/Fe-400.

Table 1. Specific Surface Area and the Gas-Sensing Performance of the As-Prepared Samples

sample name	Au (wt %)	Pt (wt %)	calcination temperature (°C)	BET surface area (m²/g)	sensitivity (S)		
					1 ppm acetone	100 ppm acetone	500 ppm acetone
Fe-250[a]	0	0	250	132.2	1.27	19.17	33.06
Fe-400[a]	0	0	400	44.29	1.67	20.87	60.03
Au/Fe-250[a]	3	0	250	65.76	4.15	37.17	67.94
Au/Fe-400[a]	3	0	400	44.52	5.91	46.38	78.30
Pt/Fe-250[b]	0	3	250	64.84	1.00	8.06	41.96
Pt/Fe-400[b]	0	3	400	46.37	1.00	9.96	56.03

[a]Sensitivity measured at 270 °C. [b]Sensitivity measured at 300 °C.

higher-temperature calcination was adopted as a standard for further investigations.

Figure 6B demonstrates the best sensor response in each case (i.e., after 400 °C calcination and at their respective optimum temperatures). All profiles exhibited a close to linear response versus acetone concentration in the testing range, but the Au/Fe-400 sample was clearly superior, particularly at low acetone concentrations (≤1 ppm), which is of interest for clinical pathology. At 1 ppm acetone, the sensitivity value of Au/Fe-400 was 5.91, which is about 4 times higher than that of Fe-400 (1.67). The former value is comparable to those obtained by Biswal[11d] (R_a/R_g = 3.65) and Chakraborty et al.[12] (R_a/R_g = 8.1). However, it should be noted that they used γ-Fe$_2$O$_3$ instead of α-Fe$_2$O$_3$. In comparison to the result for Au/α-Fe$_2$O$_3$

nanospindles as reported by Zhang et al.,[15] the Au/Fe-400 sample was significantly more sensitive at equivalent acetone concentrations, despite having a similar Au loading (~3 wt %).

Figure 7 illustrates the response−recovery curves of the sensors. Figure 7A shows the speed of reaction to the instantaneous supply and cutoff of 100 ppm acetone over a 15 s cycle. Response recovery times, defined as the time required to reach 90% of the final signal (maximum or background), were found to be rapid for all samples; the rise time (0.5 s) was typically faster than the recovery time, viz., 0.5, 10, and 20 s for Pt/Fe-400, Fe-400, and Au/Fe-400, respectively. This pattern was evident over a range of (lower) acetone levels, as presented in Figure 7B. The repeatability (absence of sensor drift), as judged by full recovery to the
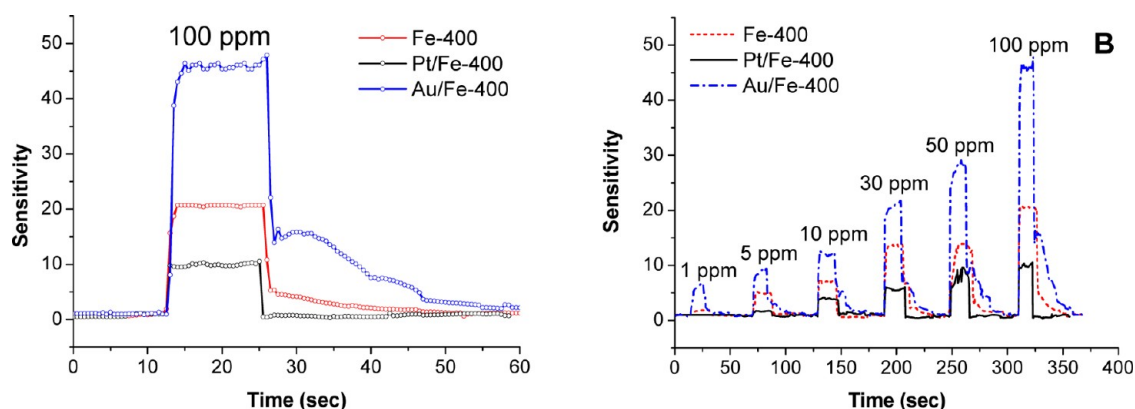
Figure 7. (A) Response−recovery characteristics toward 100 ppm acetone and (B) real-time response−recovery curves to different concentrations of acetone at the optimum operating temperature: 270 °C for Fe-400 and Au/Fe-400 and 300 °C for Pt/Fe-400.
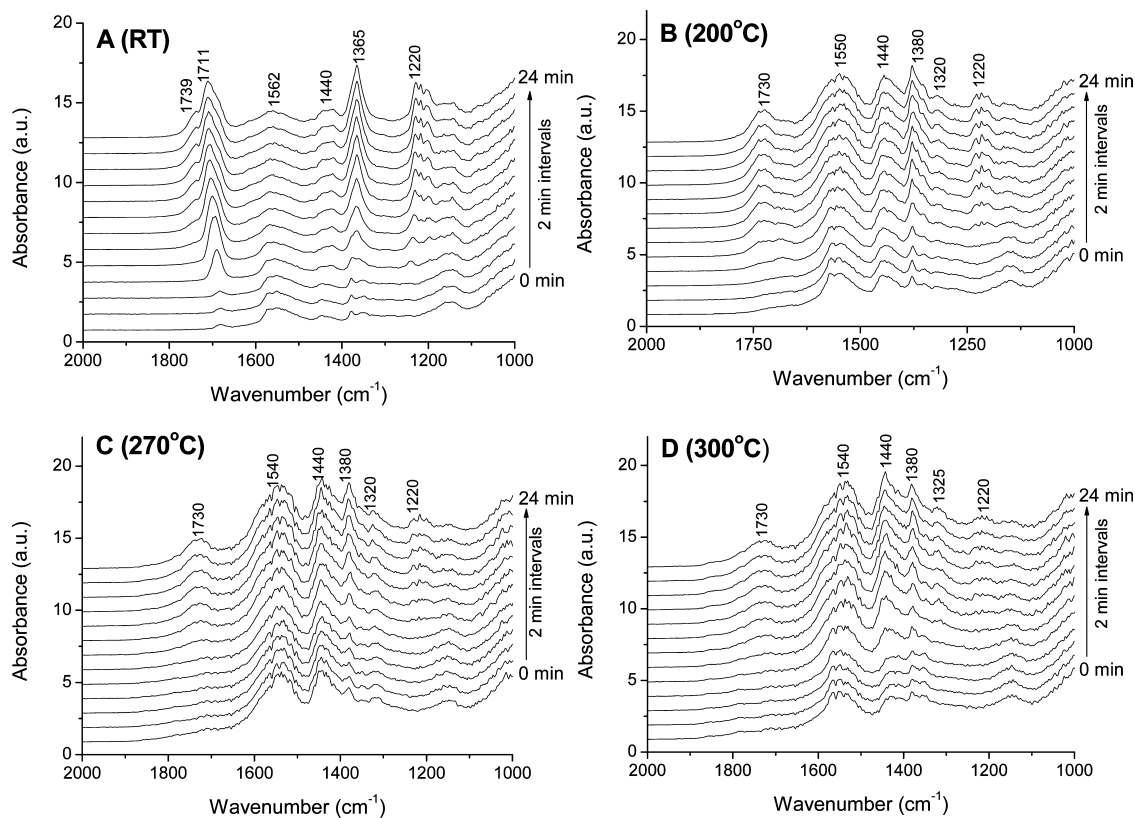

Figure 8. DRIFTS spectra (1000−2000 cm^{-1}) of acetone adsorption on Au/Fe-400 at room temperature, 200, 270, and 300 °C. Acetone vapor was generated via bubbling liquid acetone at 0 °C with a mixture of 50% air in N$_2$ gas as the carrier.

baseline response, was also good. However, the suppression in response observed by addition of Pt to the Fe-400 control is somewhat surprising in view of the known promoting effect of noble metals on semiconductor-based sensors in general.

3.3. Mechanistic Study of the Gas-Sensing Property. The relationship between the surface chemical state and the sensing mechanism toward acetone was investigated via DRIFTS. Figures 8 and 9 present real-time changes in infrared spectral details (2000−1000 and 4000−2000 cm^{-1}, respectively) recorded over Au/Fe-400 upon sustained exposure to acetone/air at different temperatures. At ambient temperature (Figure 8A), the chemisorption of acetone is clear from the carbonyl peak developing at ca. 1690 cm^{-1}, which gradually shifts to a higher frequency (1710 cm^{-1}). The later develop-

ment of a shoulder at 1739 cm^{-1} may be assigned to physically adsorbed acetone. Gas-phase acetone (Figure S4) shows that this peak is essentially at the same position (Figure S4). No evidence was seen for surface carbonate formation at this stage, a process that is unlikely to occur at room temperature. Exposing Fe-400 to pure N$_2$ as a control also resulted in a carbonyl band at 1705 cm^{-1} (Figure S4), thus indicating that only adsorption processes occur at ambient temperature. The corresponding growth of bands at 1365 and 1220 cm^{-1} (Figure 8A) and at 2920 and 2970 cm^{-1} (Figure 9A) are assigned to C−C and C−H vibrations, respectively, which confirms that the molecular integrity of acetone is maintained.

The involvement of isolated surface OH groups in the above chemisorption process is evident by the gradual disappearance
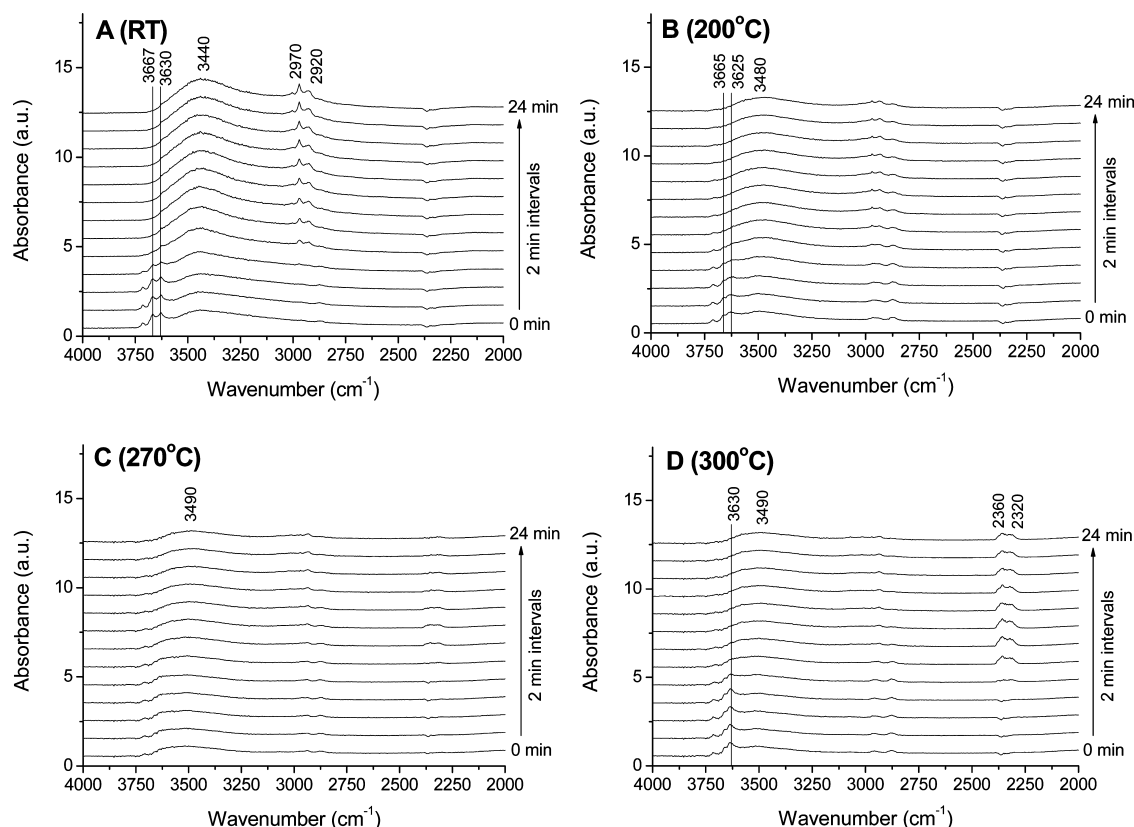
Figure 9. DRIFTS spectra (2000−4000 cm^{-1}) of acetone adsorption on Au/Fe-400 at room temperature, 200, 270, and 300 °C. Acetone vapor was generated via bubbling liquid acetone at 0 °C with a mixture of 50% air in N$_2$ gas as the carrier.

of their characteristic bands at 3630, 3670, and 3710 cm^{-1} (Figure 9A). The surface OH groups may be involved in the chemisorption process via two routes: (i) they interact with acetone molecules via hydrogen bonding as reported in the case of Fe$_2$O$_3$[21] and (ii) they promote the adsorption and activation of molecular oxygen by synergistic interaction with O vacancies (vide infra).

Major spectral changes were observed during a 30 min exposure of Au/Fe-400 to acetone/air at elevated temperatures. At 200 °C (Figure 8B), new bands appeared almost instantaneously at ~1550 and 1440 cm^{-1}, characteristic of the asymmetric and symmetric COO$^-$ stretching vibrations of surface acetate, a likely partial oxidation product.[22] This implies the dissociative chemisorption of acetone with C−C bond cleavage. However, because the likely coproduct is a methoxy group (−O−CH$_3$) exhibiting a methyl-symmetric deformation at around 1445−1430 cm^{-1},[21] the unambiguous assignment of bands in this range is difficult. The more gradual evolution of IR bands at 1730 and 1220 cm^{-1} corresponds to the asymmetric and symmetric bends of CO$_2$ adsorbed in the bent configuration, a quite labile species.[23] This assignment is borne out by the observation that these bands weaken at higher temperature (Figure 9C,D) whereas bands characteristic of CO$_2$ gas develop at 2360 and 2320 cm^{-1}. In contrast, two pairs of bands at 1550/1320 and 1440/1380 cm^{-1}, assigned as bidentate and monodentate carbonates, respectively, tend to increase in line with their more stable properties.

The corresponding DRIFT spectra of Fe-400 and Pt/Fe-400 are presented in Figures S5 and S6, respectively. At 200 °C, it can be seen that after equal times of exposure to acetone (30 min) the Au/Fe-400 sample (Figure 8B) exhibits the strongest

IR bands of adsorbed acetate at 1550 and 1440 cm^{-1}. Thus, the presence of Au clearly promotes the catalytic conversion of acetone molecules. In contrast, the presence of Pt nanoparticles promotes the generation of more CO$_2$ gas, especially at elevated temperature (270 and 300 °C, Figure S6).

The similarity in spectral features over all samples (Figures 8, 9, S5, and S6) indicates that the deposition of either Au or Pt does not generate a new reaction pathway for the conversion of acetone molecules on α-Fe$_2$O$_3$. However, Au/Fe-400 and Pt/Fe-400 are found to be better at breaking the C−C bond in acetone molecules than Fe-400, leading to the formation of various surface cleavage species including CO$_2$ molecules. A possible surface reaction mechanism is thus proposed on the basis of the above observations, as shown in Figure 10.

However, the above results still do not fully account for the superior sensitivity of Au-decorated α-Fe$_2$O$_3$ toward acetone molecules, especially at high temperatures near 300 °C. The sensor sensitivity (S) is defined as $S = R_a/R_g$, where R_a is the sensor resistance in air and R_g is the resistance in the reducing target gas. With regard to surface oxide species and oxygen activation, it is known that, even in the less-reducible TiO$_2$ oxide, O-vacancy sites are able to adsorb molecular O$_2$ whereas the perfect TiO$_2$ surface (free of O vacancies) cannot.[24] In our previous report, we have demonstrated that TiO$_2$ supports with the highest OH group regeneration ability also exhibit the best catalytic performance in several oxidation reactions.[25] Considering the higher reducibility of α-Fe$_2$O$_3$, we find that this leads to more abundant O vacancies and thus more adsorption of molecular O$_2$. This phenomenon is found to occur more in the temperature range of 200−300 °C.
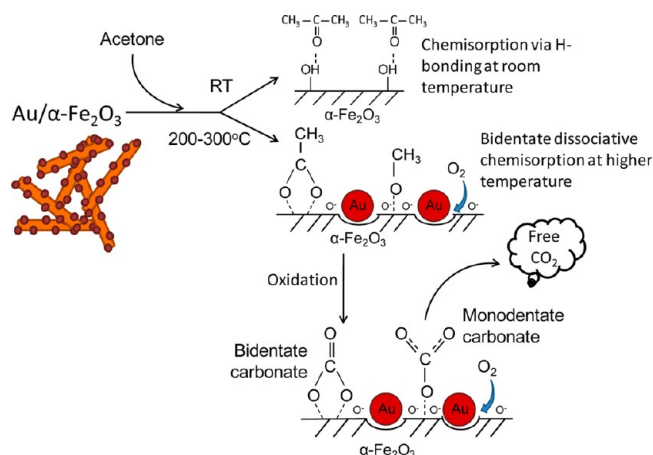
Figure 10. Schematic diagram of the surface reaction mechanism of acetone on Au-deposited α-Fe$_2$O$_3$.

Figure 11. (A) TG curves of Au/Fe-400 and Pt/Fe-400 in 2.5% CO and Fe-400 in 5% H$_2$. (B) FTIR profiles of Au/Fe-400 and Pt/Fe-400 tested in 2.5% CO. A Sample (20 mg) was exposed to 2.5% CO in Ar at 30 mL/min at a heating rate of 10 °C/min to 700 °C. For FTIR measurement, the absorbance spectrum at 4 cm^{-1} resolution in the range of 4000−400 cm^{-1} (midrange MCT detector) was stored every minute (120 coadded scans), from which the recovery of CO$_2$ was monitored by the area under the bending vibration centered at ∼670 cm^{-1}. The conversion of CO was monitored by a diminution of the area under the fundamental stretching envelope centered at ∼2140 cm^{-1}.

To determine the oxygen activity in α-Fe$_2$O$_3$, the in situ TG-FTIR analysis of Au/Fe-400 and Pt/Fe-400 in CO gas was carried out. CO molecules can react with oxygen species to form CO$_2$ molecules, which are easily monitored by FTIR. For comparison, the reduction of α-Fe$_2$O$_3$ (Fe-400) in 5% H$_2$ was also carried out. As shown in Figure 11A, samples Au/Fe-400 and Pt/Fe-400 under CO exhibit weight losses in the same temperature range (250−320 °C) as for the reduction of α-Fe$_2$O$_3$ in H$_2$, which is known to correspond to the conversion of α-Fe$_2$O$_3$ to Fe$_3$O$_4$.[26] Figure 11B confirms that the extraction of lattice O proceeds with the release of CO$_2$ gas. Such a degree of reduction can occur only if bulk oxygen ions (O^{2-}) migrate to the reactive surface. Because this temperature range straddles the values verified for optimum sensor response, it is clear that lattice oxygen (in α-Fe$_2$O$_3$) is involved in the sensing mechanism.

Although the lattice oxygen species becomes active at around 300 °C in the above samples, the sustained supply of molecular oxygen is crucial to a continuous sensing performance. Lee et al. observed the formation of p-type conductivity and the ordering of the oxygen vacancies in α-Fe$_2$O$_3$ nanowires due to strong surface adsorption resulting from the high content of oxygen vacancies and the large surface-to-volume ratio.[27] Wang et al. observed that in ethanol sensing experiments the sensor displayed a p-type characteristic below 50 ppm ethanol and an n-type characteristic for higher concentrations.[28] In our acetone sensing experiments, an n-type characteristic is always exhibited at 270 °C (Figure 7), indicating that the charge carriers are mainly negatively charged oxygen species that form a depletion layer at the nanorod surface, a phenomenon known to be more pronounced in nanosized materials.[28] In this case, the fast supply and conversion of molecular oxygen species into lattice oxygen and the high mobility of the latter should lead to high sustained sensitivity to acetone molecules. Thus, the role of Au in amplifying the sensor response is to activate molecular oxygen better to replenish lattice O as it is consumed. This is supported by the fact that the main difference between Au/Fe-400 and Pt/Fe-400 is a strong CO$_2$ peak below 50 °C in the former, which is absent in the latter, which can be observed in Figure 11B. In our previous report,[26] we also observed that there is no such low-temperature CO$_2$ peak in the pure α-Fe$_2$O$_3$ support. Because it is well known that supported Au catalysts can catalyze CO oxidation at very low temperatures,[29] we conclude th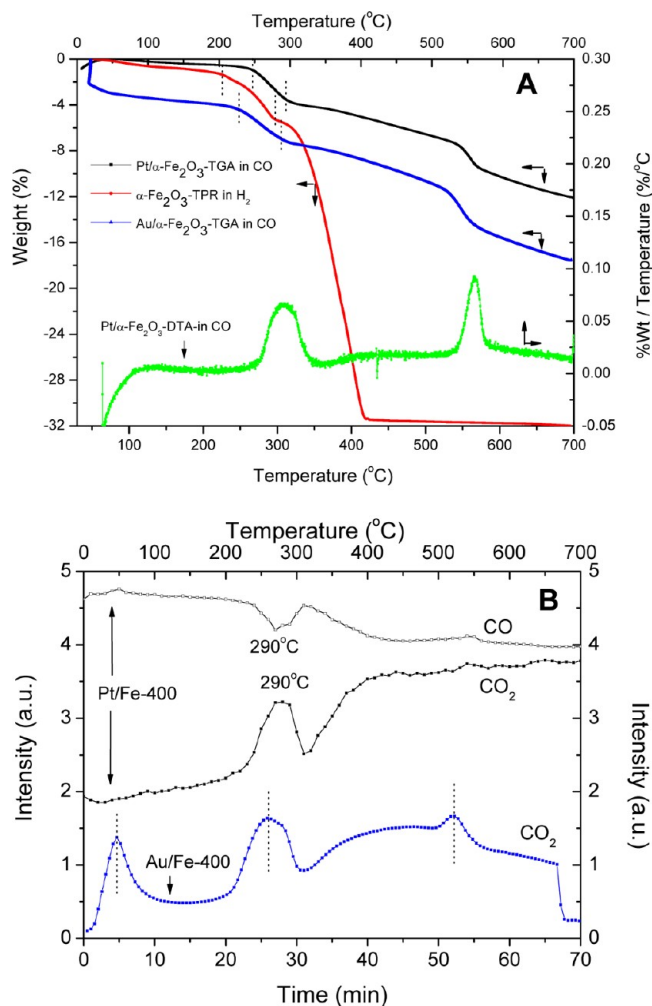at in the presence of Au nanoparticles some oxygen species become extremely active. Elsewhere, Li et al. have proposed that Au nanoparticles significantly increase the quantity of active oxygen ions via the catalytic dissociation of molecular oxygen.[30] Haruta and Takeda et al. believe that the active sites for active oxygen formation and CO oxidation should be located at or near the perimeter interface between the Au nanoparticles and the metal oxide.[31,32] The Au nanoparticles are probably deposited at or near the oxygen vacancies. Because of the presence of Au nanoparticles on metal oxides, a Schottky barrier is formed, which generates a depleting electron region at the interface, thus facilitating the dissociation of molecular oxygen.[19a,30] For Pt/Fe-400, although it is active in breaking the C−C bond in acetone molecules, its ability to activate molecular oxygen is evidently inferior to that of nanosized Au. Table 2 summarizes the relative performance of the various samples for acetone sensing in light of these considerations.

Table 2. Possible Sensing Mechanism of Acetone Involving Oxygen Activation on Different Samples

sample	low temperature	high temperature
Au/α-Fe$_2$O$_3$	activation of molecular O$_2$ is easy;	high activity of lattice oxygen;
	low activity of lattice oxygen;	fast supply and conversion of O$_2$ into lattice oxygen;
	slow decomposition of acetone;	more-active oxygen species;
	low sensitivity	fast decomposition of acetone; high sensitivity
α-Fe$_2$O$_3$ and Pt/α-Fe$_2$O$_3$	activation of molecular O$_2$ is difficult;	high activity of lattice oxygen;
	low activity of lattice oxygen;	slow supply and conversion of O$_2$ into lattice oxygen;
	slow decomposition of acetone;	less-active oxygen species;
	low sensitivity	fast decomposition of acetone; low sensitivity
	The sensing performance is controlled by the activation of O$_2$ molecules as the oxygen supply.	

4. CONCLUSIONS

An ultrahigh-sensitivity material for acetone detection, based on porous Au-decorated 1D α-Fe$_2$O$_3$, has been prepared via a facile microwave irradiation method. It exhibits a close to linear response and fast dynamics in response/recovery cycling over a wide range of acetone concentration. The optimum sensing temperature was found to be 270 °C. The sensing mechanism, elucidated by DRIFTS, involves the dissociative adsorption of acetone, promoted by Au and Pt nanoparticles, followed by rapid partial oxidation to acetate. Au is superior to Pt in promoting the molecular oxygen activation to replenish mobile lattice oxygen in α-Fe$_2$O$_3$ directly consumed in the oxidation reaction. These results will probably aid in the development of a new type of sensor toward organic molecules with much enhanced sensitivities.

■ ASSOCIATED CONTENT

⑤ Supporting Information

TEM images of the mixture of TEAOH and Fe(NO$_3$)$_3$ at room temperature without microwave irradiation. BJH desorption pore size distribution profiles of Fe-250 and Fe-400. TGA profile and FTIR spectra of as-prepared FeOOH. DRIFTS spectra of acetone vapor in N$_2$ and in air and its adsorption on Fe-400, Au/Fe-400, and Pt/Fe-400 at room temperature. This material is available free of charge via the Internet at http://pubs.acs.org.

■ AUTHOR INFORMATION

Corresponding Author
*E-mail: liqiuhong2004@hotmail.com and zhong_ziyi@ices.a-star.edu.sg.

Notes
The authors declare no competing financial interest.

■ ACKNOWLEDGMENTS

■ REFERENCES

(1) Teo, J. S. K.; Teh, S. P.; Addiego, W. P.; Zhong, Z.; Borgna, A.; Truitt, R. E. *Int. J. Hydrogen Energy* **2011**, *36*, 5763−5774.

(2) Feldmann, C. *Adv. Mater.* **2001**, *13*, 1301−1303.

(3) (a) Wang, Z. Y.; Luan, D. Y.; Madhavi, S.; Li, C. M.; Lou, X. W. *Chem. Commun.* **2011**, *47*, 8061−8063. (b) Brezesinski, K.; Haetge, J.; Wang, J.; Mascotto, S.; Reitz, C.; Rein, A.; Tolbert, S. H.; Perlich, J.; Dunn, B.; Brezesinski, T. *Small* **2011**, *7*, 407−414.

(4) (a) Hao, Q.; Liu, S.; Yin, X.; Du, Z.; Zhang, M.; Li, L.; Wang, Y.; Wang, T.; Li, Q. *CrystEngComm* **2011**, *13*, 806−812. (b) Huang, J.; Yang, M.; Gu, C.; Zhai, M.; Sun, Y.; Liu, J. *Mater. Res. Bull.* **2011**, *46*, 1211−1218. (c) Patil, D.; Patil, V.; Patil, V. *Sens. Actuators, B* **2011**, *152*, 299. (d) Abaker, M.; Umar, A.; Baskoutas, S.; Dar, G. N.; Zaidi, S. A.; Al-Sayari, S. A.; Al-Hajry, S. A.; Kim, S. H.; Hwang, S. W. *J. Phys. D* **2011**, *44*, 425401.

(5) (a) Xiong, Y.; Li, Z.; Li, X.; Hu, B.; Xie, Y. *Inorg. Chem.* **2004**, *43*, 6540−6542. (b) Woo, K.; Lee, H. J.; Ahn, J. P.; Park, Y. S. *Adv. Mater.* **2003**, *15*, 1761−1764. (c) Jia, C.-J.; Sun, L.-D.; Yan, Z.-G.; You, L.-P.; Luo, F.; Han, X.-D.; Pang, Y.-C.; Zhang, Z.; Yan, C.-H. *Angew. Chem., Int. Ed.* **2005**, *44*, 4328−4333. (d) Zhong, Z.; Lin, M.; Ng, V.; Ng, G. X. B.; Foo, Y.; Gedanken, A. *Chem. Mater.* **2006**, *18*, 6031−6036.

(6) Zhong, Z.; Ho, J.; Teo, J.; Shen, S.; Gedanken, A. *Chem. Mater.* **2007**, *19*, 4776−4782.

(7) Ma, J. M.; Teo, J.; Mei, L.; Zhong, Z.; Li, Q. H.; Wang, T. H.; Duan, X.; Lian, J; Zheng, W. *J. Mater. Chem.* **2012**, *22*, 11694−11700.

(8) (a) Leadbeater, N. E. *Chem. Commun.* **2005**, *23*, 2881−2902. (b) Galema, S. A. *Chem. Soc. Rev.* **1997**, *26*, 233−238.

(9) (a) Panda, A. B.; Glaspell, G.; El-Shall, M. S. *J. Am. Chem. Soc.* **2006**, *128*, 2790−2791. (b) Zhu, Y.-J.; Wang, W.-W.; Qi, R.-J.; Hu, X.-L. *Angew. Chem., Int. Ed.* **2004**, *43*, 1410−1414.

(10) Hu, X.; Yu, J. C. *Adv. Funct. Mater.* **2008**, *18*, 880−887.

(11) (a) Jing, Z.; Wu, S. *Mater. Lett.* **2006**, *60*, 952−956. (b) Hu, X.; Yu, J. C.; Gong, J.; Li, Q.; Li, G. *Adv. Mater.* **2007**, *19*, 2324−2329. (c) Wang, Y.; Cao, J.; Wang, S.; Guo, X.; Zhang, J.; Xia, H.; Zhang, S.; Wu, S. *J. Phys.Chem. C* **2008**, *112*, 17804−17808. (d) Biswal, R. C. P. *Sens. Actuators, B* **2011**, *157*, 183−188. (e) Jing, Z. H. *Mater. Sci. Eng. A* **2006**, *441*, 176−180.

(12) Chakraborty, S.; Banerjee, D.; Ray, I.; Sen, A. *Curr. Sci.* **2008**, *94*, 237−242.

(13) (a) Tassopoulos, C. N.; Barnett, D.; Fraser, T. R. *Lancet* **1969**, *293*, 1282−1286. (b) Kundu, S. K.; Bruzek, J. A.; Nair, R.; Judilla, A. M. *Clin. Chem.* **1993**, *39*, 87−92.

(14) Kung, M. C.; Davis, R. J.; Kung, H. H. *J. Phys. Chem. C* **2007**, *111*, 11767−11775.

(15) Zhang, J.; Liu, X. H.; Wang, L. W.; Yang, T. L.; Guo, X. Z.; Wu, S. H.; Wang, S. R.; Zhang, S. M. *J. Phys. Chem. C* **2011**, *115*, 5323−5357.

(16) (a) Zhong, Z.; Lin, J.; Teh, S. P.; Teo, J.; Dautzenberg, F. M. *Adv. Funct. Mater.* **2007**, *17*, 1402−1408. (b) Zhong, Z.; Patskovskyy, S.; Bouvrette, P.; Luong, J. H. T.; Gedanken, A. *J. Phys. Chem. B* **2004**, *108*, 4046−4052.

(17) Yin, X. M.; Li, C. C.; Zhang, M.; Hao, Q. Y.; Liu, S.; Li, Q. H.; Chen, L. B.; Wang, T. H. *Nanotechnology* **2009**, *20*, 455503.

(18) Chemseddine, A.; Moritz, T. *Eur. J. Inorg. Chem.* **1999**, *1999*, 235−245.

(19) (a) Liu, X. H.; Zhang, J.; Guo, X. Z.; Wu, S. H.; Wang, S. R. *Nanotechnology* **2010**, *21*, 095501. (b) Tang, B.; Wang, G.; Zhuo, L.; Ge, J.; Cui, L. *Inorg. Chem.* **2006**, *45*, 5196−5200.

(20) Yamazoe, N.; Sakai, G.; Shimanoe, K. *Catal. Surv. Asia* **2003**, *7*, 63−75.

(21) Socrates, G. *Infrared Characteristic Group Frequencies: Tables and Charts*, 2nd ed.; John Wiley & Sons: Chichester, U.K., 1994.

(22) (a) Griffiths, D. M.; Rochester, C. H. *J. Chem. Soc., Faraday Trans. 1* **1977**, *73*. (b) Rochester, C. H.; Topham, S. A. *J. Chem. Soc, Faraday Trans. 1* **1979**, *75*.

(23) (a) Payen, E.; Grimblot, J.; Lavalley, J. C.; Daruti, M.; Mauge, F. Vibrational Spectroscopy in the Study of Oxide (Excluding Zeolites) and Sulfide Catalysts. In *Handbook of Vibrational Spectroscopy*; Chalmers, J. M., Griffiths, P. R., Eds.; John Wiley & Sons: Chichester, U.K., 2002; Vol. *4*, pp 3005−3041. (b) Busca, G.; Lorenzelli, V. *Mater. Chem* **1982**, *7*, 89−126.

(24) Wahlström, E.; Vestergaard, E. K.; Schaub, R.; Rønnau, A.; Vestergaard, M.; Lægsgaard, E.; Stensgaard, I.; Besenbacher, F. *Science* **2004**, *303*, 511−513.

(25) Zheng, Z.; Teo, J.; Chen, X.; Liu, H.; Yuan, Y.; Waclawik, E. R.; Zhong, Z.; Zhu, H. *Chem.—Eur. J.* **2010**, *16*, 1202−1211.

(26) Zhong, Z.; Highfield, J.; Lin, M.; Teo, J.; Han, Y.-F. *Langmuir* **2008**, *24*, 8576−8582.

(27) Lee, Y.-C.; Chueh, Y.-L.; Hsieh, C.-H.; Chang, M.-T.; Chou, L.-J.; Wang, Z. L.; Lan, Y.-W.; Chen, C.-D.; Kurata, H.; Isoda, S. *Small* **2007**, *3*, 1356−1361.

(28) Wang, C.; Wang, F.-F.; Fu, X.-Q.; Zhang, E.-D.; Xu, Z. *Chin. Phys. B* **2011**, *20*, 050701.

(29) Haruta, M.; Kobayashi, T.; Sano, H.; Yamada, N. *Chem. Lett.* **1987**, *16*, 405−408.

(30) Li, C. C.; Li, L. M.; Du, Z. F.; Yu, H. C.; Xiang, Y. X.; Yuan, L. Y.; Cai, Y.; Wang, T. H. *Nanotechnology* **2008**, *19*, 035501.

(31) Fujitani, T.; Nakamura, T. *Angew. Chem., Int. Ed.* **2011**, *123*, 10326−10329.

(32) Kuwauchi, Y.; Yoshida, H.; Akita, T.; Haruta, M.; Takeda, S. *Angew. Chem., Int. Ed.* **2012**, *51*, 7729.